

Luminous solar neutrinos I: Dipole portals

Ryan Plestid^{1,2,*}

¹*Department of Physics and Astronomy, University of Kentucky Lexington, KY 40506, USA*

²*Theoretical Physics Department, Fermilab, Batavia, IL 60510, USA*

Solar neutrinos upscattering inside the Earth can source unstable particles that can decay inside terrestrial detectors. Contrary to naive expectations we show that when the decay length is much shorter than the radius of the *Earth* (rather than the detector), the event rate is independent of the decay length. In this paper we study a transition dipole operator (neutrino dipole portal) and show that Borexino's existing data probes previously untouched parameter space in the 0.5–20 MeV regime, complementing recent cosmological and supernova bounds. We briefly comment on similarities and differences with luminous dark matter and comment on future prospects for analogous signals stemming from atmospheric neutrinos.

I. INTRODUCTION

The Earth is constantly pelted with neutrinos from the Sun (among other sources), and dark matter from our local galaxy; both can serve as a resource with which to search for new physics. The canonical strategy, as it pertains to dark matter, is to detect particles directly via elastic or inelastic scattering within a detector, however this strategy applies equally well to new physics coupled via some neutrino-portal. For example, electron recoil data can be used to constrain both elastic and transition neutrino dipole moments, both of which have attracted recent interest as potential explanations of the XENON1T excess [1–5] (see also [6] for a review). More broadly speaking, a transition dipole operator can serve as “dipole portal” to a dark sector [7–9] and is described by the interaction Lagrangian¹

$$\mathcal{L}_{\text{int}} \supset d_a \bar{N}_R \sigma_{\mu\nu} \nu_L^{(a)} F^{\mu\nu} = \frac{\mu_\nu^{(a)}}{2} \bar{N}_R \sigma_{\mu\nu} \nu_L F^{\mu\nu}. \quad (1)$$

The index $a = e, \mu, \tau$ denotes the neutrino flavour and N_R is a (possibly Dirac or Majorana) sterile neutrino. The dipole operator, d_a , can generically be flavour dependent however since the solar neutrino flux contains all three flavors the sensitivity derived here is only mildly flavor dependent. This model was proposed as a phenomenological explanation of the MiniBooNE and LSND anomalies [10], and subsequently studied in the context of radiative muon capture [11], supernovae cooling [8], collider searches [8], double bangs at ICECUBE [12], fixed-target facilities [8, 13–15], low-recoil dark matter detectors [16] and cosmology of the early universe [9]. This paper is the first in a series of two that investigates the physics potential for detecting upscattered unstable particles sourced by solar neutrinos inside the Earth with a neutrino dipole portal serving as a useful benchmark

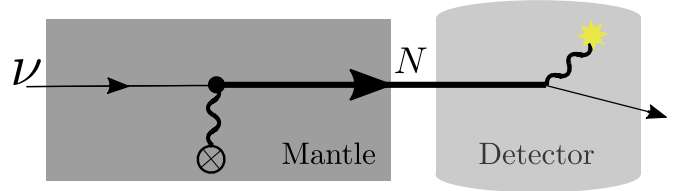


FIG. 1. Upscattering of a solar neutrino inside the Earth’s mantle (or core, or crust) leads to a “heavy” $O(\text{MeV})$ sterile neutrino, N . In the weak coupling limit N is long-lived, and can propagate long distances eventually decaying inside a large-scale detector. For a neutrino-dipole portal this leads to a deposited photon with an energy of order $\sim 100 \text{ keV} - 10 \text{ MeV}$.

example. In [17] we consider a mass-mixing portal whose upscattering and decay phenomenology is sufficiently different to warrant an isolated treatment. where

The parametric sensitivity to the dipole operator, d , of a search strategy that uses a flux of incident neutrinos *directly* is straightforward. The rate of scattering events inside a detector is proportional to the flux times the cross section $\Phi \times \sigma$ multiplied by the number of targets inside the detector’s fiducial volume. The flux of incident neutrinos is independent of d , while the detection cross section scales quadratically with the dipole operator, $\sigma \sim d^2$. Finally, the event rate is determined. The signal rate, R , therefore scales as $R \sim d^2$ which is advantageous for small values of d relative to the d^4 scaling we discuss below. Another possibility is to make use of astrophysical fluxes *indirectly* by leveraging their ability to *produce* a flux of new physics particles. For instance, cosmic rays interacting in the upper atmosphere can produce long-lived particles in much the same way dedicated fixed target facilities (e.g. NA62 [18], SHiP [19] etc.) can: pp and/or pA collisions source mesons, which promptly decay, ultimately producing a flux of light, long-lived, new physics particles e.g. heavy neutral leptons [20], light dark matter [21], or millicharged particles [22]. Such an indirect production mechanism costs an extra two powers of the coupling constant, such that for a neutrino dipole-portal the flux itself scales as d^2 leading to an event rate that scales as d^4 . These indirect fluxes are therefore ex-

* rpl225@uky.edu

¹ We use the variable d rather than μ_ν throughout this work. A quick conversion factor that is convenient for comparing results across conventions is $d \times 6.75 \text{ MeV} = \mu_\nu / \mu_B$ with μ_B the Bohr magneton.

pected to provide meaningful sensitivity to new physics only at moderately small couplings.

A seemingly innocuous twist on this latter scenario is to consider detecting an indirect flux using decays inside a detector. Consider a detector with a characteristic length scale ℓ , and a particle with a decay length, λ , that satisfied $\lambda \gg \ell$. Because a long-lived particle is unlikely to decay inside a finite sized detector, $P_{\text{dec}} = 1 - \exp[-\ell/\lambda] \approx \ell/\lambda \sim d^2$, naively the signal rate in this scenario scales as d^4 .

The parametric dependence of the signal changes dramatically, however, if the decay length satisfies $\lambda \ll R_{\oplus}$ and the indirect flux is sourced by upscattering inside the Earth as opposed to meson decays or other “prompt” sources localized in e.g. the upper atmosphere. The reason for this is that the upscattered flux that arrives at the detector becomes proportional to λ in such a way that $\Phi \times P_{\text{dec}}$ is independent of λ at leading order. This can be understood as the effective column density of targets growing with λ in such a way as to precisely cancel the $1/\lambda$ penalty arising from the rarity of decays within the detector. This effect persists until it is saturated by the boundaries of the Earth after which, rather than being suppressed by a factor that is $O(\ell/\lambda)$ the rate is instead suppressed by a factor that is $O(R_{\oplus}/\lambda)$.

We can make our discussion more concrete by considering a flux of incident particles on a thick slab of material of length L_{slab} which terminates in a detector as depicted in Fig. 1. If we consider an infinitesimally thin slice of the slab (thickness dz) then the flux of long-lived particles, N , arriving at the front detector is $d\Phi_N = \Phi_{\nu\odot} \bar{n}_A \sigma_{\nu\rightarrow N} e^{-z/\lambda} dz$, where z is the distance from the slice to the detector, \bar{n}_A is the number density of upscattering targets and $\sigma_{\nu\rightarrow N}$ is the upscattering cross section for $\nu A \rightarrow NA$. Integrating over z we find the flux at the detector is given by

$$\begin{aligned} \Phi_N &= \Phi_{\nu\odot} \bar{n}_A \sigma_{\nu\rightarrow N} \int_0^{L_{\text{slab}}} e^{-z/\lambda} dz \\ &= \Phi_{\nu\odot} [\bar{n}_A \lambda] \sigma_{\nu\rightarrow N} (1 - e^{-L_{\text{slab}}/\lambda}) , \end{aligned} \quad (2)$$

where the quantity in the square braces can be interpreted as the effective column density of scatterers along the line of sight. The rate of decays within the detector will be proportional to the product of this flux, the area of the detector, and the probability of decaying within it

$$\begin{aligned} R_{\text{dec}} &= \Phi_N A_{\text{det}} (1 - e^{-\ell/\lambda}) \\ &\approx \Phi_{\nu\odot} V_{\text{det}} \bar{n}_A \sigma_{\nu A \rightarrow NA} , \end{aligned} \quad (3)$$

where we have assumed $L_{\text{slab}} \gg \lambda \gg \ell$. This can be compared to the rate of quasi-elastic scattering $\nu X \rightarrow X\nu$ signal events from the *direct* flux of neutrinos

$$R_{\text{el}} = \Phi_{\nu\odot} V_{\text{det}} n_X \sigma_{\nu X \rightarrow NX} . \quad (4)$$

We have included the label X , because for scattering events to be visible inside the detector, their energy deposition must be observable as X -recoil energy. Because

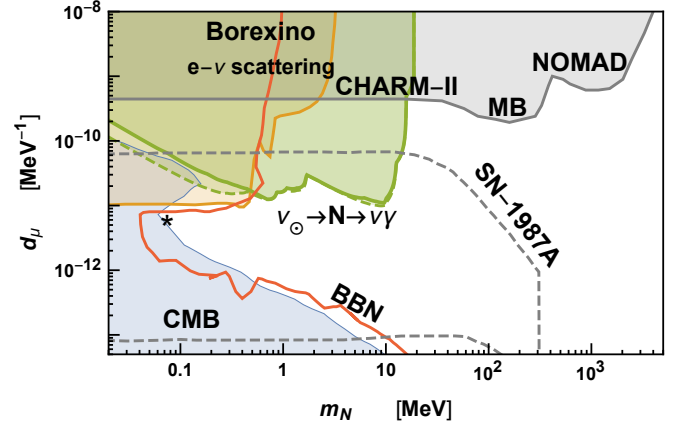


FIG. 2. Constraints on a muon-only dipole coupling d_μ , from cosmology (BBN and CMB) [9], SN-1987A [8], Borexino $e\nu$ scattering data [9, 23, 24], CHARM-II $e\nu$ scattering data [12, 25], MiniBooNE [8, 26], and NOMAD [13, 27]; the last viable parameter space [9] to explain the XENON1T excess is indicated with a star. This work ($\nu_\oplus \rightarrow N \rightarrow \nu\gamma$) is shown in green with a solid (dashed) line for a Dirac (Majorana) N . Constraints were obtained by multiplying the solar neutrino flux by $P_{e\mu}(E_\nu)$ [28–30].

low-energy nuclear recoils are very difficult to observe, this means that $\nu e \rightarrow Ne$ scattering often provides better constraints since the electron recoil energy is more easily observed than the nuclear recoil energy. Upscattering off of electrons, however, has a much smaller cross section than $\nu A \rightarrow NA$. In upscatter-decay scenarios, the nuclear recoil of a target inside the Earth does not need to be detected, and so $\nu A \rightarrow NA$ scattering is an ever-present production mechanism which always dominates because the cross section is coherent.

We see that despite the upscattered flux being indirect (i.e. sourced by scattering) the event rate is parametrically identical to direct detection (scaling as d^2 rather than d^4). Furthermore, one can clearly see a number of avenues via which event rates from upscattered long-lived particles can supersede those of direct elastic recoil:

1. While both event rates are proportional to the volume of the detector, R_{dec} scales with the density of upscattering targets *inside the Earth*. The interior of the Earth tends to be 3-12 times more dense than detector material.
2. The cross sections entering the two expressions are different, and the upscattering cross section may be much larger. For example $\nu e \rightarrow Ne$ (detection) has a much smaller cross section than $\nu A \rightarrow NA$ (upscattering).
3. Direct detection may be kinematically disfavoured, as emphasized in the literature surrounding luminous dark matter [31–33].

Even when $\nu X \rightarrow Nx$ scattering is kinematically allowed, points 1. and 2. can make the decay event rate much

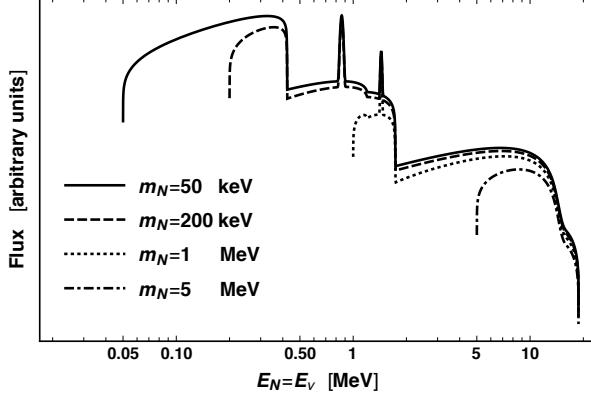


FIG. 3. Shape of sterile neutrino flux, $\Phi_N \propto \Phi_{\nu\odot} \times \sigma_{\nu \rightarrow N}^{\sim}$, for various choices of m_N *c.f.* Fig. 12. For a flavor dependent dipole portal d_a the flux should be multiplied by a factor of $P_{ea}(E_\nu)$ survival/transition probability.

larger than the elastic scattering event rate. The rest of this paper is dedicated to investigating the sensitivity of large-scale detectors to a dipole portal for $m_N \leq 18.8$ MeV, the cut-off of the solar-neutrino flux. Our results are summarized and shown in context with other constraints for a muon-only dipole portal in Fig. 2; constraints derived in this paper for d_e and d_τ are broadly similar, while constraints based on fixed-target facilities either weaken or disappear entirely because the flux considered is predominantly composed of muon neutrinos. This is the first of two papers on the possible detection of solar neutrinos that upscatter within the Earth’s mantle. In [17] a qualitatively similar, but phenomenologically distinct scenario is discussed where $\nu \rightarrow N$ proceeds via a mass-mixing portal subsequently decaying into an electron-positron pair.

The paper is organized as follows: In Section II we discuss the upscattering of solar neutrinos into unstable right-handed neutrinos via the dipole portal. Next, in Section III we discuss decay properties including the difference between Majorana and Dirac decays [34–36]. Then, in Section IV, we discuss how these two pieces of phenomenology conspire to produce photon spectra at large-scale detectors on Earth, the details of which are determined by the geometry of the Earth relative to the Sun, and the latitude of the detector. In Section V we use the photon spectra derived in Section IV to set lim-

its on a dipole portal couplings using Borexino [23, 24] and Super-Kamiokande data [37]. We conclude with Section VI where we summarize our main results, emphasize the overlap between luminous dark matter searches and luminous solar neutrino searches, and comment on qualitative effects that are important for future dedicated analysis.

II. DIPOLE-PORTAL UPSCATTERING

Solar neutrinos never exceed 20 MeV in energy, and this means that their (hypothetical) electromagnetic interactions with nuclei fall firmly in the coherent regime $F(Q^2) \approx 1$. Moreover, the four-momentum transfer is limited by E_ν , and so the recoil energy of a nucleus, A , never exceeds $T_A^{\max} \sim (20\text{MeV})^2/m_A \lesssim 10$ keV. Therefore, neutrino-up-scattering on nuclei can be reliably approximated by considering the nucleus as a fixed and static charge density sourcing a Coulomb field. Within this approximation $E_N = E_\nu$ by energy conservation and the matrix element for up-scattering is given by

$$\langle |\mathcal{M}|^2 \rangle = \frac{4d^2(Ze)^2}{t} [4E_\nu^2 - m_N^2 + m_N^4/t], \quad (5)$$

where flavour indices have been suppressed for brevity’s sake. Using $d\sigma = \frac{1}{16\pi^2} \langle |\mathcal{M}|^2 \rangle d\Omega$ (appropriate for potential scattering), noting that $dt = 2E_\nu^2 d\cos\theta$, and integrating over the azimuthal angle we have

$$\begin{aligned} \frac{d\sigma}{dt} &= \frac{4d^2 Z^2 (4\pi\alpha)}{16\pi} \frac{1}{t} [4E_\nu^2 - m_N^2 + m_N^4/t] \\ &= \frac{(dZ\alpha)^2}{t} [4E_\nu^2 - m_N^2 + m_N^4/t]. \end{aligned} \quad (6)$$

This is logarithmically enhanced to prefer forward scattering such that it is a good approximation to treat the resultant “beam” of steriles produced via solar neutrino upscattering to be parallel with the solar neutrino flux. We restrict upscattering to “forward” angles satisfying $\cos\theta > 0$ such that (for $Q^2 = -t$)

$$Q_{\min}^2 = (P_\nu - P_N)^2 = (E_\nu - \sqrt{E_\nu^2 - m_N^2})^2 \quad (7)$$

$$Q_{\max}^2 = P_\nu^2 + P_N^2 = 2E_\nu^2 - m_N^2. \quad (8)$$

and clearly in the $E_\nu \gg m_N$ limit this give the result $Q_{\min} = \frac{1}{2}m_N^2/E_\nu$ and $Q_{\max} \approx 2E_\nu^2$. We can then calculate the rate of “forward” scattering (denoted by the superscript \sim) as

$$\begin{aligned} \sigma_{\nu \rightarrow N}^{\sim} &= 4Z^2 \alpha d^2 \left[\log \left(\frac{Q_{\max}^2}{Q_{\min}^2} \right) + \frac{1}{4} \frac{m_N^4}{E_\nu^2 Q_{\min}^2} - \frac{1}{4} \frac{m_N^2}{E_\nu^2} \log \left(\frac{Q_{\max}^2}{Q_{\min}^2} \right) - \frac{1}{4} \frac{m_N^4}{E_\nu^2 Q_{\max}^2} \right] \Theta(E_\nu - m_N) \\ &\approx 4Z^2 \alpha d^2 \left[\log \left[\frac{(2E_\nu)^4}{m_N^4} \right] + 1 - \log 2 + O(\epsilon^2 \log \epsilon) \right] \Theta(E_\nu - m_N). \end{aligned} \quad (9)$$

The terms in the top line have been organized based on their scaling with respect to $\epsilon = m_N/E_\nu$. At

leading-log accuracy in ϵ , we therefore have $\sigma \sim$

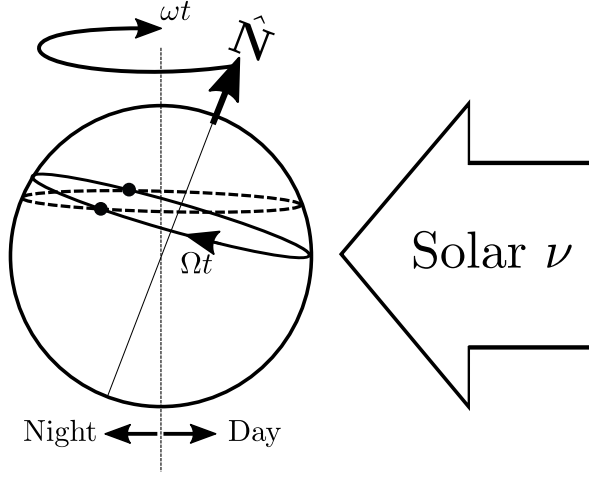


FIG. 4. Time dependent motion of a detector relative to the solar neutrino flux. A detector at a fixed latitude traces out a path depicted by the solid line [$\Omega - \omega = 2\pi/(1 \text{ day})$ and $\omega = 2\pi/(365 \text{ days})$].

$16Z^2\alpha d^2 \log(2E_\nu/m_N)$ with corrections being of order $\sim \text{few } \%$ for $\epsilon < 1/2$. The Z^2 enhancement means that scattering from nuclei will always dominate over scattering from electrons. Keeping only the leading-logarithm and taking $d = 1.97 \cdot 10^{-9} \text{ MeV}^{-1}$ [a convenient choice for decay-length purposes *c.f.* Eq. (20)]

$$\sigma_{\nu \rightarrow N}^{\sim} \approx [1.76 \cdot 10^{-40} \text{ cm}^2] Z^2 \log(2E_\nu/m_N). \quad (10)$$

For $E_\nu \gtrsim m_N$ (near threshold) one must use the full expression in the first line of Eq. (9) and the resultant flux is shown for a few benchmark masses in Fig. 3.

The flux of steriles Φ_N emerging from an infinitesimal slab of thickness dz with target density \bar{n}_A is then given by

$$d\Phi_N(E_N) = (\bar{n}_A \times dz) \sigma_{\nu \rightarrow N}^{\sim} \Phi_{\nu\odot}(E_\nu). \quad (11)$$

This flux, unsculpted by the energy dependent decay length, is plotted in Fig. 3.

For flavor dependent couplings oscillation effects should be included in the solar neutrino spectrum and the result should be summed over flavors appropriately

$$R(E_\gamma) = V_{\text{det}} \bar{n}_A \int_{m_N}^{18.8 \text{ MeV}} dE_N (1 - e^{-L_{\text{slab}}/\lambda}) \Phi_{\nu\odot}(E_\nu = E_N) \sigma_{\nu \rightarrow N}^{\sim}(E_N) \times \begin{cases} \text{box}(E_\gamma, E_N) & \text{Majorana} \\ \text{tri}(E_\gamma, E_N) & \text{Dirac} \end{cases}. \quad (18)$$

This form is applicable to a spatially varying density profile if we make the replacement $\bar{n}_A(1 - e^{-L_{\text{slab}}/\lambda}) \rightarrow \frac{1}{\lambda} \int dz \bar{n}_A(z)(1 - e^{-z/\lambda})$.

weighted by d_a^2 . This leads to, at most, an $O(1)$ modification of the constraints and we neglect it hereafter.

III. RADIATIVE STERILE DECAY

Once the flux of N 's has been calculated the resultant spectral shape of the photons from $N \rightarrow \nu\gamma$ can be calculated. The shape is somewhat model dependent, being determined by the Majorana vs Dirac nature of N which determines the angular dependence of the differential decay rate in the rest frame of N

$$\frac{d\Gamma}{d\cos\theta} \propto (1 + \alpha \cos\theta) \quad \alpha \in [-1, 1]. \quad (12)$$

A Majorana N has $\alpha = 0$, whereas a Dirac N (naively favoured to suppress dipole contributions to neutrino textures) has $\alpha = -1$ [34–36, 38]. In the lab frame, for an N with energy E_N , this leads to

$$d\Gamma/dE_\gamma = \begin{cases} \text{box}(E_\gamma, E_N) & \text{Majorana} \\ \text{tri}(E_\gamma, E_N) & \text{Dirac} \end{cases}, \quad (13)$$

where

$$\text{box}(E_\gamma) = \frac{\Theta(E_\gamma - E_\gamma^{(-)})\Theta(E_\gamma^{(+)} - E_\gamma)}{E_\gamma^{(+)} - E_\gamma^{(-)}} \quad (14)$$

$$\text{tri}(E_\gamma) = 2 \frac{E_\gamma^{(+)} - E_\gamma}{E_\gamma^{(+)} - E_\gamma^{(-)}} \text{box}(E_\gamma) \quad (15)$$

$$E_\gamma^{(\pm)} = \frac{E_\nu}{2} \left(1 \pm \sqrt{1 - \frac{m_N^2}{E_\nu^2}} \right). \quad (16)$$

The photon energy spectrum is then obtained by integrating over E_N weighted by the flux of N . For example for the Dirac N we have

$$\frac{dR(E_\gamma)}{dz} = (1 - e^{-\ell/\lambda})(1 - e^{-z/\lambda}) \times \int dE_N \frac{d\Phi_N(E_N)}{dz} \text{tri}(E_\gamma, E_N). \quad (17)$$

Taking the density to be constant, $\bar{n}_A(z) = \bar{n}_A$, integrating over z , treating $\ell \ll \lambda$, and multiplying by the size of the detector we arrive at

We have implicitly assumed that $\Phi_{\nu\odot}(E_\nu)$ is independent of z . This assumption can be violated if d is flavour non-universal ($d_e \neq d_\mu \neq d_\tau$), which is exactly true if

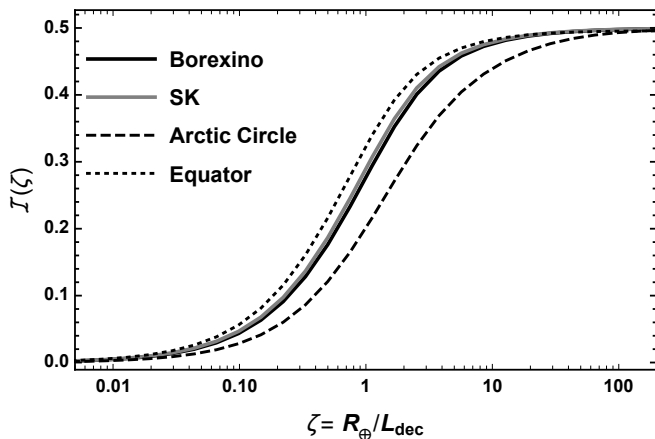


FIG. 5. $\mathcal{I}(\zeta)$ (averaged over a year) for different latitudes.

the dipole operator is flavour universal, but needn't be true if it is not. Neutrino oscillations spoil this picture in principle, but for solar neutrinos the incident flux is a statistical mixture of $O(1):O(1):O(1)$ for $\nu_e:\nu_\mu:\nu_\tau$. Constraints from solar neutrino fluxes are therefore insensitive to the flavour dependence of the coupling constants aside from $O(1)$ effects due to e.g. only 1/3 of the solar flux contributing to upscattering.

Omnipresent in our current discussion is the decay length λ whose relative size determines whether our signal scales as d^2 or d^4 . The lifetime of N is given by

$$\Gamma = \sum_a \frac{d_a^2 m_N^3}{4\pi} \times \begin{cases} 1 & \text{Dirac} \\ 2 & \text{Majorana} \end{cases}, \quad (19)$$

and its decay length, $\lambda = \gamma\beta\tau$ is therefore

$$\begin{aligned} \lambda &= \frac{4\pi}{\sum_a d_a^2 m_N^3 m_N} \sqrt{1 - \frac{m_N^2}{E_N^2}} \\ &= R_\oplus \left[\frac{1.97 \times 10^{-9} \text{ MeV}^{-1}}{d_{\text{eff}}} \right]^2 \left[\frac{1 \text{ MeV}}{m_N} \right]^4 \\ &\quad \times \left[\frac{E_N}{10 \text{ MeV}} \right] \sqrt{\frac{1 - m_N^2/E_N^2}{0.99}}. \end{aligned} \quad (20)$$

where $d_{\text{eff}} = \sum_a d_a^2$.

It turns out that the values of d and m_N that lead to a roughly Earth-scale decay length are right at the boundary of currently unexplored parameter space.

IV. SIGNALS AT LARGE SCALE DETECTORS

Unlike the simple picture presented in the introduction, the “slab” of Earth that is traversed by solar neutrinos in transit to a terrestrial detector is time dependent. This is obvious in that during the day the solar neutrinos pass through the Earth's crust whereas at night the majority of the line-of-sight density they encounter is the

Earth's mantle. This can be visualized by working in a coordinate system where the solar flux is incident from the \hat{x} direction. In this frame, the Earth rotates about its axis daily, and precesses about the \hat{z} axis yearly as depicted in Fig. 4.

Let us highlight a number of qualitative effects

- There is a stark day-night asymmetry with almost no signal during the day and all of the signal coming at night. The seasonal variation is less extreme being an $O(1)$ effect.
- The neutrinos only pass through the core of the Earth², which is composed of high-density and high- Z material, during winter for detectors in the northern hemisphere. Since $\Phi_N \propto Z^2 \bar{n}_A$, and the core is a high-density, high- Z material this also introduces an important seasonal modulation.
- The direction of the photons will be highly correlated with the zenith angle for highly boosted N 's (most of the spectrum).

Many of these issues are discussed in detail in [33] for inelastic dark matter, which also has mostly-forward up-scattering. For our present purposes we will focus on the time-averaged rate of photon deposition in a given experiment, and we therefore ignore details of seasonal and daily signal modulation. Furthermore, we consider a simplified model of the Earth that is designed to give a conservative estimate of the photon yield, while remaining (nearly-)analytically tractable.

We take the Earth to be a uniform sphere composed of one atomic species with $Z = Z_{\text{eff}}$ and number density \bar{n}_A , designed to mimic the average density of the Earth's mantle as shown in Appendix B. We assume that $\lambda \gg$ few km, such that the detector is effectively on the surface. Each day the detector traces out the path labeled by the frequency Ω in Fig. 4. The length of the slab through which the neutrinos pass (shown as a dashed circle in Fig. 4) changes each day such that the factor of $(1 - e^{-L_{\text{slab}}/\lambda})$ in Eq. (18) is replaced by

$$\mathcal{I}_i(\lambda) = \left\langle 1 - e^{-L(t)/\lambda} \right\rangle_i. \quad (21)$$

where i labels the i^{th} day of the year. The function $\mathcal{I}_i(\lambda)$ can be evaluated numerically, but also has simple analytic limits. For $\lambda \ll R_\oplus$ we have the intuitive result that

$$\mathcal{I}_i(\lambda) \approx \frac{t_{\text{night}}^i}{24 \text{ h}} \quad \lambda \ll R_\oplus, \quad (22)$$

such that, as was discussed in Section I, the rate of photons is independent of the decay length. Averaging over a full year's exposure would then yield a factor of 1/2

² This is important for $\lambda \gtrsim R_\oplus$. If $\lambda \ll R_\oplus$ then particles upscattered in the core will decay before reaching the detector.

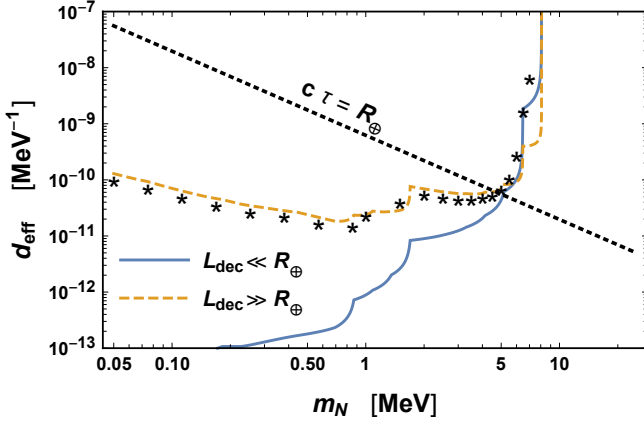


FIG. 6. Comparison of exclusions obtained using Eqs. (27) to (29). We can see that the prescription of Eq. (31) provides a good estimate of the exclusion curve. .

because of the absence of signal during the day. In the opposite limit, where $\lambda \gg R_\oplus$, the function is simply related to the average column density seen by the neutrinos

$$\mathcal{I}_i(\lambda) \approx \frac{1}{\lambda} \langle L(t) \rangle_i \quad \lambda \gg R_\oplus. \quad (23)$$

Making use of the seasonal modulation in signal could

serve as a powerful tool for characterizing backgrounds and substantially improve the sensitivity of large terrestrial detectors as discussed in [33] for the case of inelastic dark.

For simplicity, we ignore seasonal variations and focus here on the total integrated rate, or equivalently the time averaged rate taken over a full year of run time. This has the advantage of being directly comparable to publicly released data from Borexino. For this purpose we can define the average rate for the full live-time of an experiment as

$$\bar{R}(E_\gamma) = \langle R(E_\gamma) \rangle_{\text{year}} = \frac{1}{365} \sum_{i=1}^{365} R_i(E_\gamma), \quad (24)$$

where $R_i(E_\gamma)$ is defined the same way as in Eq. (18) but with the replacement $(1 - e^{-L_{\text{slab}}/\lambda}) \rightarrow \mathcal{I}_i(\lambda)$. This leads immediately to the function

$$\mathcal{I}(\zeta) = \frac{1}{365} \sum_{i=1}^{365} \mathcal{I}_i(\zeta), \quad (25)$$

where we have introduced $\zeta(E_N, m_N, d) = R_\oplus/\lambda$. The quantity $\mathcal{I}(\zeta)$ has a mild latitude dependence as illustrated in Fig. 5. With this function defined we can express the year-averaged differential rate of photon deposition, $\bar{R}(E_\gamma)$ (per unit time per unit energy) as

$$\bar{R}(E_\gamma) = V_{\text{det}} \bar{n}_A \int_{m_N}^{18.8 \text{ MeV}} dE_N \mathcal{I}(\zeta) \Phi_{\nu\odot}(E_\nu = E_N) \sigma_{\nu \rightarrow N}^{\leftrightarrow}(E_N) \times \begin{cases} \text{box}(E_\gamma, E_N) & \text{Majorana} \\ \text{tri}(E_\gamma, E_N) & \text{Dirac} \end{cases}. \quad (26)$$

In the limit where $\lambda \ll R_\oplus$, but $\lambda \gg h$ (with h the overburden) we can replace $\mathcal{I}(\zeta) \rightarrow \frac{1}{2}$ (half of the exposure is day-time where there is no signal³). If instead $\lambda \gg R_\oplus$ such that $\zeta \rightarrow 0$, then we can replace $\mathcal{I}(\zeta) \rightarrow \langle L(t) \rangle / \lambda$ such that for the two limits we have

$$\frac{d\bar{R}}{dE_\gamma} = (104 \text{ Hz}) \left[\frac{V_{\text{det}} \bar{n}_A}{10^{30}} \right] \left[\frac{Z_{\text{eff}}}{12} \right]^2 \cdot \begin{cases} \left[\frac{d_{\text{eff}}}{1.97 \cdot 10^{-9} \text{ MeV}^{-1}} \right]^2 \cdot \frac{1}{2} \frac{dR_{\ll}}{dE_\gamma} & \lambda \ll R_\oplus \\ \left[\frac{d_{\text{eff}}}{1.97 \cdot 10^{-9} \text{ MeV}^{-1}} \right]^4 \cdot \left[\frac{m_N}{1 \text{ MeV}} \right]^4 \cdot \left[\frac{\langle L(t) \rangle}{R_\oplus} \right] \frac{dR_{\gg}}{dE_\gamma} & \lambda \gg R_\oplus \end{cases} \quad (27)$$

$$\frac{dR_{\ll}}{dE_\gamma} = \int_{m_N}^{18.8 \text{ MeV}} dE_N \left[\frac{\Phi_{\nu\odot} \bar{\sigma}}{10^{-30} \text{ Hz}} \right] \times \begin{cases} \text{box}(E_\gamma, E_N) & \text{Majorana} \\ \text{tri}(E_\gamma, E_N) & \text{Dirac} \end{cases} \quad (28)$$

$$\frac{dR_{\gg}}{dE_\gamma} = \int_{m_N}^{18.8 \text{ MeV}} dE_N \left[\frac{10 \text{ MeV}}{E_N} \right] \sqrt{\frac{0.99}{1 - m_N^2/E_N^2}} \left[\frac{\Phi_{\nu\odot} \bar{\sigma}}{10^{-30} \text{ Hz}} \right] \times \begin{cases} \text{box}(E_\gamma, E_N) & \text{Majorana} \\ \text{tri}(E_\gamma, E_N) & \text{Dirac} \end{cases}, \quad (29)$$

where $\Phi_{\nu\odot} = \Phi_{\nu\odot}(E_\nu = E_N)$, and we have introduced a

reference cross section,

$$\begin{aligned} \bar{\sigma} &= \sigma_{\nu \rightarrow N}^{\leftrightarrow} \left[\frac{1.97 \cdot 10^{-9} \text{ MeV}^{-1}}{d} \right]^2 \left[\frac{1}{Z^2} \right] \\ &\sim O(1) \times 10^{-40} \text{ cm}^2, \end{aligned} \quad (30)$$

³ If $\lambda \lesssim h$ then production in the Earth's crust (rather than the mantle) and there will be signal both day and night.

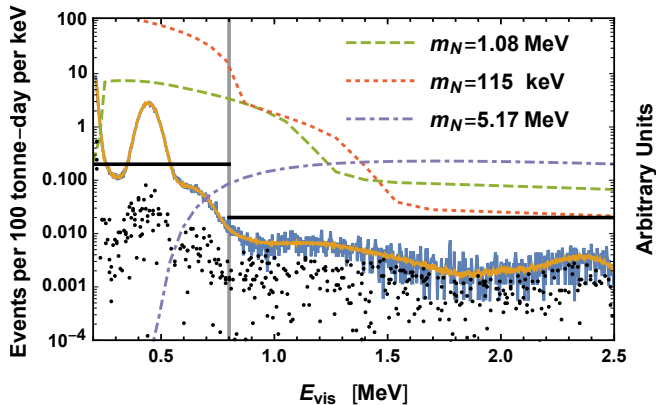


FIG. 7. Data from Borexino’s low-energy region as presented in [23, 24]. The vertical band shows our binning into low-energy region I and low-energy region II, and the horizontal black lines correspond to the average rate used in each region to set our exclusions. Photon spectral shapes (Dirac N) are shown for three different masses. .

that is independent of d and Z , but depends on m_N and E_ν as described in Eq. (9).

The function dR_{\ll}/dE_γ is proportional to the differential rate of photons produced per target nucleus A , and is left unsculpted by the dependence of λ on E_N . In contrast, the function dR_{\gg}/dE_γ is sculpted by $\lambda(E_N) \propto 1/P_N$, because the rate depends on the ratio $\langle L(t) \rangle / \lambda$; up-scattered N ’s with more energy are less likely to decay inside the detector.

The most important feature of Eq. (27) is the transition between d^2 and d^4 scaling. The interpolation between these two limits is given by Eq. (26), which can be safely used over the entire $m_N - d$ plane of parameter space. It is, however, instructive to consider experimental sensitivity in the two limits shown in Eq. (27). A reasonable approximation is to calculate exclusions assuming $\lambda \gg R_\oplus$ and $\lambda \ll R_\oplus$ and to use the weakest of the two limits at a given value of m_N . Explicitly, if we derive constraints $d < d_{\gg}(m_N)$ and $d < d_{\ll}(m_N)$ then we can approximate the full constraint, $d < d_\zeta(m_N)$ derived using Eq. (26), by

$$d_\zeta(m_N) \approx \text{Max}[d_{\gg}(m_N), d_{\ll}(m_N)] . \quad (31)$$

Dedicated analyses at large scale detectors should include core of the Earth, the radial dependence of the mantle density, photon spectral information, and make use of time-modulation to discriminate backgrounds from signal. At this level of detail it becomes mandatory to use Eq. (26) rather than Eq. (27) (especially in the cross-over region between the two limits). As is shown in Fig. 6 for the case of the Borexino low-energy region (LER), at our working level of precision Eq. (31) is sufficient for the conservative limit setting done in this paper. Our results using obtained using Eq. (31) are shown for a Dirac neutrino in Fig. 8 and for a Majorana neutrino in Fig. 9.

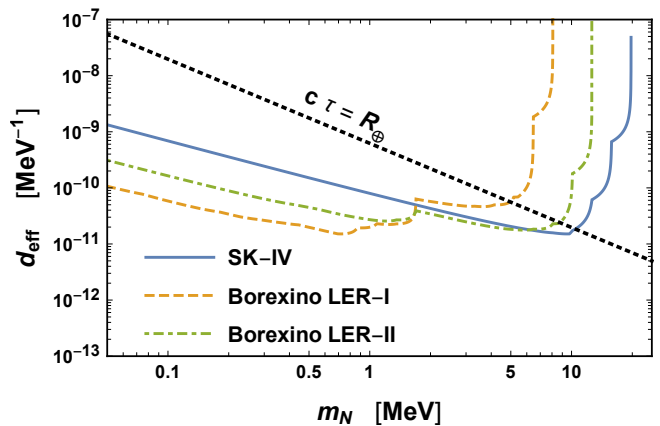


FIG. 8. Exclusions from the three experimental data-sets considered in this work for a Dirac N (triangular distribution) calculated using Eq. (31). The regions above the lines are excluded. The diagonal line shows where the cross-over between $\lambda \gg R_\oplus$ and $\lambda \ll R_\oplus$ is expected to take place. We assume a simplified model of the earth with a uniform density, $\bar{n}_A = 1.03 \text{ cm}^{-3}$, and a $Z_{\text{eff}} = 11.8$. For comparisons to other probes of neutrino-dipole portals see Fig. 2.

V. NEW CONSTRAINTS ON DIPOLE PORTALS

We consider data from Borexino and Super-Kamiokande to set constraints on a neutrino dipole portal. We perform an (extremely) conservative analysis on the Borexino low-energy region (LER) data set from [23] (available online at [24]), binning their data into a region with $E_{\text{vis}} < 0.8 \text{ keV}$ (LER-I) and a region with $E_{\text{vis}} > 0.8 \text{ keV}$ (LER-II). Since the efficiency of Borexino is so high and photons are reconstructed nearly identically to electrons we neglect efficiencies in our estimates (setting them equal to one). Our signal’s photon spectrum is very broad and so we do not include the effects of the $O(50 \text{ keV})$ broadening from the detector resolution as this will be a negligible effect. Our analysis is (up to a coarse re-binning) a rate-only analysis and so is insensitive to spectral shape details.

For Super-Kamiokande we use recent results from SK-IV, taking Fig. 14 of [37] *after* cuts were applied. Photon events are difficult to distinguish from electron or positron events since the radiation length of an MeV photon is tens of centimeters, and so pair produces rapidly in medium. The cuts applied on the SK-IV data involved external event vetoes and a tight fiducial volume cut [37]. Since the decay length of N is four to five orders of magnitude larger than the Super-Kamiokande detector, we would expect the photons to be uniformly distributed throughout the detector volume and so these cuts do not modify the expected rate normalized to fiducial volume. To set limits on d_{eff} we require that the $N \rightarrow \nu\gamma$ do not produce a signal in excess of the observed rate above 4 MeV, which we calculate to be 4.62 events per kton-day. We do not make use of any spectral shape information,

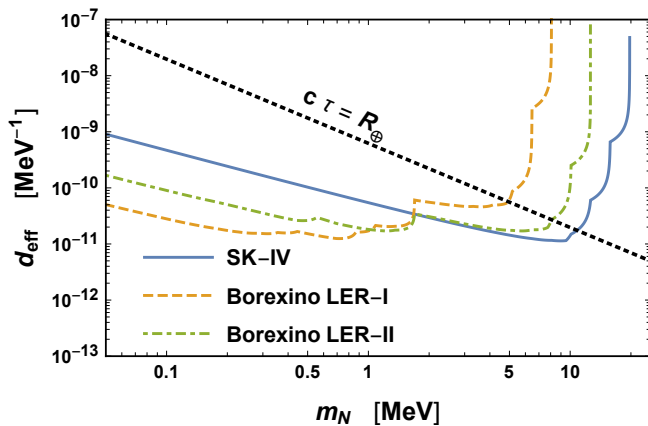


FIG. 9. Same as Fig. 8 but for a Majorana N (box distribution and double the decay rate) calculated using Eq. (31).

day-night asymmetry, or zenith angle dependence all of which could be leveraged for improved sensitivity in a dedicated analysis.

VI. CONCLUSIONS

The presence of solar neutrinos and coherent upscattering with the high-density, and moderate- Z material of the Earth's mantle can lead to a dramatic flux of sterile neutrinos passing through terrestrial detectors. These fluxes are so large that they compensate for the relatively low probability of decay within the detector volume resulting in rates that dominate over elastic scattering by orders of magnitude.

As we explore in [17], similar phenomenology can be used to study other upscattering processes such as $\nu \rightarrow N$ via a mass-mixing portal, followed by $N \rightarrow \nu e^+ e^-$. The phenomenology differs qualitatively from the dipole-scattering example, however, because the upscattering process is quasi-isotropic in the lab frame. This eliminates day-night asymmetry to a first approximation, and requires a slightly re-worked treatment. We refer the interested reader to [17] where these details are dis-

cussed and similar bounds are worked out from the non-observation of energetic e^+e^- pairs are Borexino and Super-Kamiokande.

Unsurprisingly, luminous neutrino signals share many of the same qualitative features with luminous dark matter. The signal rate is independent of detector composition depending only on the volume of the detector, scattering is preferentially forward, and the signal modulates in time. While similarities exist, there are also important differences. Luminous dark matter is expected to be heavy $m_\chi \sim 1$ TeV, with a mass-splitting of $O(100$ keV) and a non-relativistic velocity [33]. This means that the resultant photons are monochromatic with an energy set by the mass-splitting, and that threshold effects are important⁴. In contrast the model considered in this paper leads to moderately relativistic sterile neutrinos, whose lab-frame photon distribution is therefore broadened. The solar neutrino flux is broad, and since neutrinos are much lighter than nuclei, the only threshold effect that manifests itself in this work is the requirement that $E_\nu \geq m_N$. Looking forward it is important to emphasize that *any* astrophysical source of neutrinos (e.g. atmospheric) could produce similar phenomenology, albeit with the potential mandatory inclusion of neutrino oscillation effects. Luminous signals of inelastic transitions within the Earth have many common ingredients, but their signatures inside detectors can be somewhat model dependent.

Our study further motivates a dedicated program at future large scale detectors to search for upscattered new physics within the Earth. This includes inelastic dark matter, but also any neutrinophilic inelastic transition. Such a program would leverage zenith-dependence, time-modulation, and spectral shape characteristics to distinguish new physics from backgrounds.

Our study has demonstrated the discovery potential using solar neutrinos, but heavier sterile neutrinos, N , can be produced from atmospheric neutrinos and it would be interesting to study their impact on dipole portals and other inelastic upscattering operators. Future experiments such as JUNO and Hyper-Kamiokande can serve as sensitive probes of upscattered particles, as can any other large-volume detector capable of detecting MeV scale photons (this statement is independent of detector density). Searches could also leverage time modulation, which needs to be studied in more detail as has been done for luminous dark matter [33].

Finally, we have focused on solar neutrinos, which we have shown to be a powerful tool with which to study a dipole portal connecting active neutrinos to a sterile state with mass $m_N \lesssim 20$ MeV. Atmospheric neutrinos have a much smaller flux, but could probe heavier m_N , where constraints are lacking as shown in Fig. 2.

Experiment.	[MeV]		[Events per kton-day]
	E_{\min}	E_{\max}	
Borexino LER-I	0.2	0.8	1.2
Borexino LER-II	0.8	2.5	0.57
Super-Kamiokande IV	4.49	15.5	4.62

TABLE I. Summary of experimental data used in setting constraints in this paper. Taken from Fig. 2 of [23] (available online at [24]), and Fig. 14 of [37]. The excluded rate is a highly conservative choice *c.f.* Fig. 7. A proper statistical analysis, spectral shape information, and day-night asymmetry could easily improve sensitivity.

⁴ For some parameter space in [33] upscattering into the excited state is only possible if the target nucleus is very heavy e.g. ²⁰⁸Pb.

VII. ACKNOWLEDGEMENTS

I would like to thank Joachim Kopp, Vedran Brdar, Kevin Kelly, Gordan Krnjaic, and Matheus Hostert for helpful discussions, and I am especially grateful to Pedro Machado, Volodymyr Takhistov, and Ciaran Hughes for detailed comments and feedback on early versions of this manuscript. I would like to thank the Fermilab theory group for their hospitality and welcoming research atmosphere. This work was completed while visiting Fermilab with support from the Intensity Frontier Fellowship. This work was supported by the U.S. Department of Energy, Office of Science, Office of High Energy Physics, under Award Number DE-SC0019095. This manuscript has been authored by Fermi Research Alliance, LLC under Contract No. DE-AC02-07CH11359 with the U.S. Department of Energy, Office of Science, Office of High Energy Physics.

Appendix A: Calculation of $\mathcal{I}(\zeta)$

To calculate the decay-weighted average path length $\mathcal{I}(\zeta)$ we take our detector to be described by a point

$$p(t) = (\sqrt{R_\oplus^2 - z_0^2} \cos \Omega t, \sqrt{R_\oplus^2 - z_0^2} \sin \Omega t, z_0) , \quad (\text{A1})$$

defined in the reference frame of the Earth (\hat{z} parallel to the magnetic pole). We then rotate the Earth's pole via a the rotation matrix

$$R_{\text{tilt}} = \begin{pmatrix} \cos \theta_{\text{tilt}} & 0 & \sin \theta_{\text{tilt}} \\ 0 & 1 & 0 \\ -\sin \theta_{\text{tilt}} & 0 & \cos \theta_{\text{tilt}} \end{pmatrix} , \quad (\text{A2})$$

where $\theta_{\text{tilt}} = 23.5$ degrees. This gives us an Earth that is tilted and spinning about its own axis, but is static relative to the Sun. In reality the Earth precesses relative to the Sun. We therefore apply a final rotation $R_{\text{prec}}(\omega t)$ for rotation about the \hat{z}' axis (perpendicular to the Sun) ultimately arriving at the depiction shown in Fig. 4

$$p'(t) = R_{\text{prec}}(\omega t) R_{\text{tilt}} p(\Omega t) . \quad (\text{A3})$$

Next, we draw a straight line (ray) from p' to the Sun, which in the solar-beam frame is equivalent to adding $-L\hat{x}$ to p' . We then solve for the value of L for which

$$|p'(t) - L\hat{x}|^2 = R_\oplus^2 , \quad (\text{A4})$$

which is the distance to the point of intersection of the ray with the surface of the Earth closest to the Sun. The value of L is then the time-dependent slab length

$$L_{\text{slab}}(\omega t, \Omega t) = L(t) \quad \text{if} \quad L(t) \geq 0. \quad (\text{A5})$$

For a given day of the year the day-averaged rate one should make the replacement $\Omega t \rightarrow \omega t + \Omega t$ (accounting for the slow-drift in position from the Earth's precession relative to the Sun) is given by

$$\mathcal{I}_i(\zeta) = \frac{1}{2\pi} \int_0^{2\pi} d[\Omega t] \left[1 - e^{-L_{\text{slab}}/\lambda} \right] , \quad (\text{A6})$$

with $\omega t = 2\pi \times (\text{day}_i/365)$. For the year-averaged quantity used for limit setting in this paper we have

$$\mathcal{I}(\zeta) = \frac{1}{4\pi^2} \int_0^{2\pi} \int_0^{2\pi} d[\Omega t] d[\omega t] \left[1 - e^{-L_{\text{slab}}/\lambda} \right] . \quad (\text{A7})$$

Finally, in a crude two-region model of the Earth's interior, where there is a sharp boundary between the core and mantle at some radius $r < R_\oplus$, the same basic machinery can be used to estimate the time-averaged value of \bar{n}_A and Z_{eff} (which, as discussed above, will generally be time dependent for a heterogeneous model of the Earth). Let us take $p'(t) - L\hat{x}$ again, but now search for solutions of the form

$$|p'(t) - L\hat{x}|^2 = r^2 , \quad (\text{A8})$$

Molecule.	n [10^{22} cm^{-3}]	ΣZ^2	$n \times \Sigma Z^2$ [10^{24} cm^{-3}]
SiO ₂	1.81	324	5.85
MgO	2.33	208	4.85
FeO	0.28	740	2.04
CaO	0.14	464	0.64
Cr ₂ O ₃	0.01	1344	0.12
NiO	0.01	848	0.07

TABLE II. Mantle composition calculated using Table 3. of [39] and a density of $\bar{\rho} = 4 \text{ g/cm}^3$. Elements with $n_i \leq 7 \cdot 10^{19} \text{ cm}^{-3}$ are omitted.

for which there will generically be two solutions $L_{\pm}(t)$ corresponding to when the ray goes enters and exits the core. Taking the difference of these two quantities then yields the path-length that resides within the core, which we will denote L_{core} . The mantle length can then be found from the full slab-length as $L_{\text{mantle}} = L_{\text{slab}} - L_{\text{core}}$. As we will discuss in the next section, for the $\lambda \gg R_{\oplus}$ limit this information is sufficient to estimate the added flux due to the high-density, high- Z material of the Earth's core.

Appendix B: Effective composition of the Earth

Our choice of parameters for the uniform-density model of the Earth was driven by conservative considerations. First, the core of the Earth will always yield a higher-rate of $\nu \rightarrow N$ production than an equivalent volume filled with mantle, and so treating the core as if it were made of mantle will *always* underestimate the rate of N production. The average density of Earth is roughly 5.5 g/cm^3 ; we conservatively use $\bar{\rho} = 4 \text{ g/cm}^3$ in setting our limits since the parts of the earth have a lower density.

The elemental composition of the Earth is given in Table 3. of [39] and we use the DMM column, which gives the mass percentage by molecular compound. We are ultimately interested in

$$\bar{n}_A Z_{\text{eff}}^2 = \sum_i n_i \left[\sum Z^2 \right]_i, \quad (\text{B1})$$

where the bracketed sum is adding up Z^2 within the atoms of each molecular compound. This can be re-expressed in terms of the mantle density via

$$n_i = \frac{\bar{\rho}}{m_i} f_m, \quad (\text{B2})$$

where f_m is the mass fraction given in Table 3. of [39] (Bulk DMM). We can define Z_{eff}^2 via

$$Z_{\text{eff}} := \frac{\langle Z^2 \rangle}{\langle Z \rangle}, \quad (\text{B3})$$

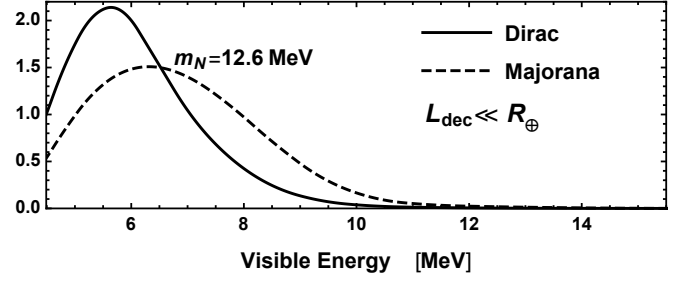


FIG. 10. Dirac vs Majorana spectral shape in the energy corresponding to the SK-IV solar neutrino dataset for a relevant benchmark mass. The condition $\lambda \ll R_{\oplus}$ is assumed corresponding to a value of d_{eff} above the dashed line in Figs. 8 and 9.

which is a density independent definition. The effective number density is then defined as

$$\bar{n}_A = \frac{\sum_i n_i [\sum Z^2]_i}{Z_{\text{eff}}^2}. \quad (\text{B4})$$

As we have shown above, for $m_N \leq 5 - 10 \text{ MeV}$, the combined sensitivity of Borexino and Super-Kamiokande probes parameter space where $\lambda \gg R_{\oplus}$. For internal consistency, we do not make use of the high-density, high- Z nature of the Earth's core in the main text, because for the higher mass regions $m_N \geq 1 - 10 \text{ MeV}$ (depending on the experiment) the parameter space being probed satisfies $\lambda \ll R_{\oplus}$. In this limit, any upscattered particles from the Earth's core would decay prior to reaching the detector and so, for limit setting purposes, including the Earth's core in the definition of the average column density is unrealistically aggressive.

For the low-mass region $m_N \lesssim 2 \text{ MeV}$, however, it is easy to include the effect of the Earth's core, since in this region $\lambda \gg R_{\oplus}$, most all of the upscattered particles will survive to the detector, and the core just serves to enhance the effective column density. The tricky part to include is the geometry of the core, which only appears along the line-of-sight to the Sun in the winter months the details of which are detector latitude dependent (see e.g. Fig. 3 of [33]). Using the procedure outlined at the end of Appendix A we estimate than for a two-component core-mantle model with $r = 0.5 R_{\oplus}$ that the $\langle L_{\text{core}}/L_{\text{slab}} \rangle \approx 0.2$ i.e. that in a full year, of the distance traversed by solar neutrinos en route to the detector, roughly twenty percent lies inside the Earth's core. The added flux from the core of the Earth can then be found by taking a weighted average of $n_A Z_{\text{eff}}^2$ in the core and mantle. Using a density for the core of 13 g/cm^3 and 4 g/cm^3 for the mantle (yielding an average density of 5.125 g/cm^3 for the Earth), and treating the core as 90% iron 10% oxygen by mass ($Z_{\text{eff}} = 24.1$ and $\bar{n}_A = 1.54 \cdot 10^{23} \text{ cm}^{-3}$). We find that the signal is enhanced by a factor of

$$\frac{0.8[\bar{n}_A Z_{\text{eff}}^2]_{\text{mantle}} + 0.2[\bar{n}_A Z_{\text{eff}}^2]_{\text{core}}}{\bar{n}_A Z_{\text{eff}}^2} \approx 2.1. \quad (\text{B5})$$

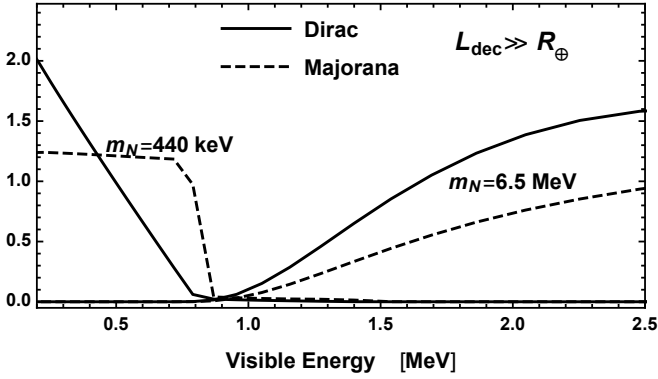


FIG. 11. Dirac vs Majorana spectral shape in the energy corresponding to the Borexino LER for two benchmark masses that can be probed using that dataset. The condition $\lambda \gg R_\oplus$ is assumed so as not to be excluded *c.f.* Figs. 8 and 9.

The effect of the core would serve to roughly double the year-averaged rate.

Appendix C: Dirac vs. Majorana

In [36, 38, 40, 41] the authors discuss the implications of a new physics discovery whose progenitor is a decaying sterile neutrino. As discussed in this paper for $N \rightarrow \nu\gamma$, the kinematic distribution of daughter particles is different depending on whether N is Dirac or Majorana. Thus, if an anomalous photon yield were to be discovered in a large volume detector, the energy spectrum of photons could be used to infer whether or not N is Dirac as op-

posed to Majorana.

In this appendix we provide a plot comparing the Dirac vs Majorana (box vs tri) spectral shapes. These shapes arise from a combination of the solar neutrino spectrum and the rest-frame decay properties of N . One also must understand the hierarchy of λ and R_\oplus , which introduces additional energy dependence in the spectrum.

Appendix D: Solar Neutrino Flux

For completeness we describe our input solar neutrino flux. This is most easily summarized in visual form in Fig. 12. The ${}^7\text{Be}$ line at 384 keV has been included but is sub-dominant to the pp and hence not visible. We treat the pep and ${}^7\text{Be}$ lines as Gaussians with a width of 10 keV.

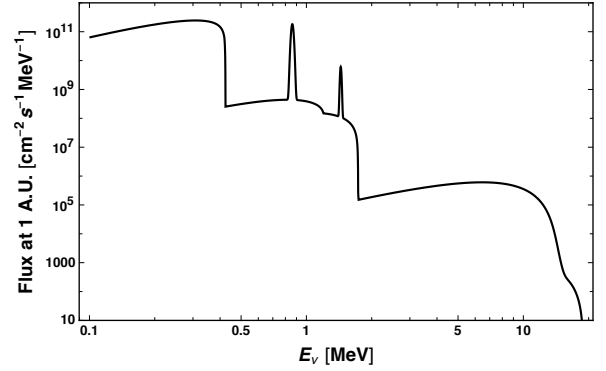


FIG. 12. Solar neutrino flux. Shapes are taken from [42] and normalizations from Tab. 2 of [43] (AGSS09 [44]).

-
- [1] Ian M. Shoemaker, Yu-Dai Tsai, and Jason Wyenberg, “An Active-to-Sterile Neutrino Transition Dipole Moment and the XENON1T Excess,” (2020), arXiv:2007.05513 [hep-ph].
 - [2] E. Aprile *et al.* (XENON), “Observation of Excess Electronic Recoil Events in XENON1T,” (2020), arXiv:2006.09721 [hep-ex].
 - [3] K.S. Babu, Sudip Jana, and Manfred Lindner, “Large Neutrino Magnetic Moments in the Light of Recent Experiments,” (2020), arXiv:2007.04291 [hep-ph].
 - [4] D. Aristizabal Sierra, R. Branada, O.G. Miranda, and G. Sanchez Garcia, “Sensitivity of direct detection experiments to neutrino magnetic dipole moments,” (2020), arXiv:2008.05080 [hep-ph].
 - [5] O.G. Miranda, D.K. Papoulias, M. Tórtola, and J.W.F. Valle, “XENON1T signal from transition neutrino magnetic moments,” Phys. Lett. B **808**, 135685 (2020), arXiv:2007.01765 [hep-ph].
 - [6] Carlo Giunti and Alexander Studenikin, “Neutrino electromagnetic interactions: a window to new physics,” Rev. Mod. Phys. **87**, 531 (2015), arXiv:1403.6344 [hep-ph].
 - [7] Alberto Aparici, Kyungwook Kim, Arcadi Santamaria, and Jose Wudka, “Right-handed neutrino magnetic moments,” Phys. Rev. D **80**, 013010 (2009), arXiv:0904.3244 [hep-ph].
 - [8] Gabriel Magill, Ryan Plestid, Maxim Pospelov, and Yu-Dai Tsai, “Dipole Portal to Heavy Neutral Leptons,” Phys. Rev. D **98**, 115015 (2018), arXiv:1803.03262 [hep-ph].
 - [9] Vedran Brdar, Admir Greljo, Joachim Kopp, and Toby Opferkuch, “The Neutrino Magnetic Moment Portal: Cosmology, Astrophysics, and Direct Detection,” (2020), arXiv:2007.15563 [hep-ph].
 - [10] Sergei N. Gninenko, “A resolution of puzzles from the LSND, KARMEN, and MiniBooNE experiments,” Phys. Rev. D **83**, 015015 (2011), arXiv:1009.5536 [hep-ph].
 - [11] David McKeen and Maxim Pospelov, “Muon Capture Constraints on Sterile Neutrino Properties,” Phys. Rev. D **82**, 113018 (2010), arXiv:1011.3046 [hep-ph].
 - [12] Pilar Coloma, Pedro A.N. Machado, Ivan Martinez-Soler, and Ian M. Shoemaker, “Double-Cascade Events from New Physics in Icecube,” Phys. Rev. Lett. **119**, 201804 (2017), arXiv:1707.08573 [hep-ph].
 - [13] S.N. Gninenko and N.V. Krasnikov, “Limits on the magnetic moment of sterile neutrino and two photon neutrino decay,” Phys. Lett. B **450**, 165–172 (1999), arXiv:hep-

- ph/9808370.
- [14] Manuel Masip, Pere Masjuan, and Davide Meloni, “Heavy neutrino decays at MiniBooNE,” *JHEP* **01**, 106 (2013), arXiv:1210.1519 [hep-ph].
 - [15] Luis Alvarez-Ruso and Eduardo Saul-Sala, “Radiative decay of heavy neutrinos at MiniBooNE and MicroBooNE,” in *Prospects in Neutrino Physics* (2017) arXiv:1705.00353 [hep-ph].
 - [16] Ian M. Shoemaker and Jason Wyenberg, “Direct Detection Experiments at the Neutrino Dipole Portal Frontier,” *Phys. Rev. D* **99**, 075010 (2019), arXiv:1811.12435 [hep-ph].
 - [17] Ryan Plestid, “Luminous Solar Neutrinos II: Mass-mixing portals,” (2020), to appear.
 - [18] Lorenza Iacobuzio, “Heavy Neutral Lepton Decay Searches at the NA62 Experiment at CERN,” (2019), presented 2019.
 - [19] C. Ahdida *et al.* (SHiP), “Sensitivity of the SHiP experiment to Heavy Neutral Leptons,” *JHEP* **04**, 077 (2019), arXiv:1811.00930 [hep-ph].
 - [20] Carlos Argüelles, Pilar Coloma, Pilar Hernández, and Víctor Muñoz, “Searches for Atmospheric Long-Lived Particles,” *JHEP* **02**, 190 (2020), arXiv:1910.12839 [hep-ph].
 - [21] James Alvey, Miguel Campos, Malcolm Fairbairn, and Tevong You, “Detecting Light Dark Matter via Inelastic Cosmic Ray Collisions,” *Phys. Rev. Lett.* **123**, 261802 (2019), arXiv:1905.05776 [hep-ph].
 - [22] Ryan Plestid, Volodymyr Takhistov, Yu-Dai Tsai, Torsten Bringmann, Alexander Kusenko, and Maxim Pospelov, “New Constraints on Millicharged Particles from Cosmic-ray Production,” (2020), arXiv:2002.11732 [hep-ph].
 - [23] M. Agostini *et al.* (BOREXINO), “Comprehensive measurement of pp -chain solar neutrinos,” *Nature* **562**, 505–510 (2018).
 - [24] **XENON1T Collaboration**, “Online data repository,” Available at https://bxopen.lngs.infn.it/wp-content/uploads/2018/10/Nature2018_Fig2b_DATA.txt (2020/09/05).
 - [25] D. Geiregat *et al.* (CHARM-II), “An Improved determination of the electroweak mixing angle from muon-neutrino electron scattering,” *Phys. Lett. B* **259**, 499–507 (1991).
 - [26] A.A. Aguilar-Arevalo *et al.* (MiniBooNE), “A Search for Electron Neutrino Appearance at the $\Delta m^2 \sim 1\text{eV}^2$ Scale,” *Phys. Rev. Lett.* **98**, 231801 (2007), arXiv:0704.1500 [hep-ex].
 - [27] J. Altegoer *et al.* (NOMAD), “The NOMAD experiment at the CERN SPS,” *Nucl. Instrum. Meth. A* **404**, 96–128 (1998).
 - [28] Evgeny K. Akhmedov, M.A. Tortola, and J.W.F. Valle, “A Simple analytic three flavor description of the day night effect in the solar neutrino flux,” *JHEP* **05**, 057 (2004), arXiv:hep-ph/0404083.
 - [29] Roni Harnik, Joachim Kopp, and Pedro A.N. Machado, “Exploring ν Signals in Dark Matter Detectors,” *JCAP* **07**, 026 (2012), arXiv:1202.6073 [hep-ph].
 - [30] Vedran Brdar, Private communication.
 - [31] Brian Feldstein, Peter W. Graham, and Surjeet Rajendran, “Luminous Dark Matter,” *Phys. Rev. D* **82**, 075019 (2010), arXiv:1008.1988 [hep-ph].
 - [32] Maxim Pospelov, Neal Weiner, and Itay Yavin, “Dark matter detection in two easy steps,” *Phys. Rev. D* **89**, 055008 (2014), arXiv:1312.1363 [hep-ph].
 - [33] Joshua Eby, Patrick J. Fox, Roni Harnik, and Graham D. Kribs, “Luminous Signals of Inelastic Dark Matter in Large Detectors,” *JHEP* **09**, 115 (2019), arXiv:1904.09994 [hep-ph].
 - [34] Robert E. Shrock, “Electromagnetic Properties and Decays of Dirac and Majorana Neutrinos in a General Class of Gauge Theories,” *Nucl. Phys. B* **206**, 359–379 (1982).
 - [35] Palash B. Pal and Lincoln Wolfenstein, “Radiative Decays of Massive Neutrinos,” *Phys. Rev. D* **25**, 766 (1982).
 - [36] A. Baha Balantekin, André de Gouvêa, and Boris Kayser, “Addressing the Majorana vs. Dirac Question with Neutrino Decays,” *Phys. Lett. B* **789**, 488–495 (2019), arXiv:1808.10518 [hep-ph].
 - [37] K. Abe *et al.* (Super-Kamiokande), “Solar Neutrino Measurements in Super-Kamiokande-IV,” *Phys. Rev. D* **94**, 052010 (2016), arXiv:1606.07538 [hep-ex].
 - [38] A. Baha Balantekin and Boris Kayser, “On the Properties of Neutrinos,” *Ann. Rev. Nucl. Part. Sci.* **68**, 313–338 (2018), arXiv:1805.00922 [hep-ph].
 - [39] Rhea K. Workman and Stanley R. Hart, “Major and trace element composition of the depleted moribund mantle (dmm),” *Earth and Planetary Science Letters* **231**, 53–72 (2005).
 - [40] Jeffrey M. Berryman, Andre de Gouvea, Patrick J. Fox, Boris Jules Kayser, Kevin James Kelly, and Jennifer Lynne Raaf, “Searches for Decays of New Particles in the DUNE Multi-Purpose Near Detector,” *JHEP* **02**, 174 (2020), arXiv:1912.07622 [hep-ph].
 - [41] Boris Kayser, “Addressing the Majorana vs. Dirac Question Using Neutrino Decays,” in *53rd Rencontres de Moriond on Electroweak Interactions and Unified Theories* (2018) pp. 323–326, arXiv:1805.07523 [hep-ph].
 - [42] J. Bahcall, “Software and data for solar neutrino research,” Available at <http://www.sns.ias.edu/~jnb/SNdata/sndata.html> (2020/09/05).
 - [43] Aldo M. Serenelli, W. C. Haxton, and Carlos Pena-Garay, “Solar models with accretion. I. Application to the solar abundance problem,” *Astrophys. J.* **743**, 24 (2011), arXiv:1104.1639 [astro-ph.SR].
 - [44] Martin Asplund, Nicolas Grevesse, A. Jacques Sauval, and Pat Scott, “The chemical composition of the Sun,” *Ann. Rev. Astron. Astrophys.* **47**, 481–522 (2009), arXiv:0909.0948 [astro-ph.SR].